ORIGINAL ARTICLE

Research on creep characteristics and variable parameter-based creep damage constitutive model of gneiss subjected to freeze–thaw cycles

Xiurong Yang[1] · Annan Jiang[1] · Fengrui Zhang[1]

Abstract

To investigate the long-term stability of surrounding rock in tunnels in cold regions, the gneiss in the Huibai tunnel of Jilin Province in China was selected for the triaxial creep test after subjecting it to freeze–thaw (F–T) cycles. Furthermore, the influence of F–T cycles on the creep properties of saturated gneiss was analyzed and discussed. The experimental results showed that the increase in the number of F–T cycles increased the creep deformation of gneiss gradually, while the creep failure stress, creep duration, and long-term strength decreased significantly. Additionally, based on the experimental results, a variable-parameter creep damage model was proposed considering the effect of F–T cycles on gneiss. The creep damage model was composed of three components: a Hooke body, a Kelvin body (parallel viscoelastic components), and a new nonlinear viscoplastic damage component. The creep damage model can not only describe the three typical creep stages (primary creep, secondary creep, and tertiary creep), but also reflect the effect of F–T damage on the creep failure stress. The comparison between the creep test curve and fitting curve of the theoretical model verified the accuracy and applicability of the model. The result of this study can provide a reference value for the support design and anti-freeze damage design for geotechnical engineering in cold areas.

Keywords Gneiss · Creep test · Damage · Long-term strength · Freeze–thaw (F–T) cycles · Northeastern china

Introduction

With the development of geotechnical engineering in the cold regions of China, geotechnical engineering affected by freezing and thawing has garnered significant attention (Grossi et al. 2007; Lin et al. 2018; Zhang et al. 2004). Rock failure does not often occur immediately after construction as it is a process that evolves gradually. Under the action of load, the stress and deformation characteristics of rock mass changes with time, i.e., the rock mass exhibits creep behavior, which is very important for the long-term stability of the project (Hamza and Stace 2018). Compared with normal geotechnical engineering, in the freezing and thawing environment, the rock mass in the cold area will repeatedly generate frost heave forces that will deteriorate the rock mass and influence the creep behavior significantly (Lai et al. 2000; Liu et al. 2019b; Xia et al. 2018). Additionally,

the long-term stability of the rock mass subjected to freezing and thawing is weakened. Therefore, studying the creep mechanical behavior of the rock mass under freeze–thaw (F–T) cycles and evaluating the time-dependent behavior will play an important role in ensuring the long-term stability of rock engineering in cold regions.

Several researchers have investigated the durability and physical–mechanical performance of rocks under F–T cycles (Bayram, 2012; Chen et al. 2004; Jamshidi et al. 2013; Karaca et al. 2010; Ke et al. 2018; Khanlari et al. 2015; Matsuoka, 1990; Mutluturk et al. 2004; Takarli et al. 2008; Tan et al. 2011; Yavuz et al. 2006). In one such study, the variation in compressive strength, elastic modulus, cohesion, and internal friction angle of granite were analyzed with respect to F–T cycles (Tan et al. 2011). The results showed that the compressive strength and elastic modulus of the granite decreased with an increase in the number of F–T cycles. The strength deterioration ratio of the rock subjected to F–T cycles is related to the pore characteristics, such as the distribution of pore sizes, pore shapes, and interconnection of pores (Khanlari et al. 2015). Moreover, the cementation of saturated samples deteriorated and generated a large

✉ Annan Jiang
  jiangannan@163.com

1 Highway and Bridge Institute, Dalian Maritime University, Dalian 116026, China

amount of secondary fractures after a single F–T cycle (Liu et al. 2018).

Regarding the study of microscopic aspects of rock mass subjected to F–T cycles, the evolution process of the pore structure in rock samples can be analyzed via computed tomography and scanning electron microscopy (SEM) (de Argandona et al. 1999; Liu et al. 2019a; Wang et al. 2019b; Yang et al. 2019). After freezing and thawing, the inner part of the rock shows surface particle detachment, crack initiation and expansion and porosity increase due to the increase in pore water volume (Park et al. 2015).

Multi-loading triaxial creep tests were performed on cataclastic rocks to study the rock creep mechanical behavior (Zhang et al. 2016). Additionally, a series of long-term creep experiments were performed on clay- and carbonate-rich horizontal and vertical shale samples by Rassouli and Zoback (2018). Hu et al. (2019) performed cyclic loading and unloading creep tests on artificial layered cemented specimens to define time-independent (instantaneous elastic and instantaneous plastic) and time-dependent (viscoelastic and viscoplastic) deformations. Based on the experimental results, many scholars suggested that there is a significant coupling characteristic between rock damage and creep, and proposed corresponding creep damage models (Hou et al. 2019; Ma et al. 2017; Qiangyong et al. 2009; Wang et al. 2019a). However, previous studies paid more attention to the constant-parameter creep constitutive model than the variable-parameter creep damage model.

The present study primarily focuses on a certain aspect of freezing and thawing properties and creep properties of rocks and does not consider the creep mechanical behavior of rocks after F–T cycles. Under seasonal alternations and alternating day and night temperatures, the time-dependent deformation of the surrounding rock continues to accumulate, which may cause instability and damage to the tunnel lining structure and affect the normal operation of the tunnel. Therefore, to understand the effect of F–T cycles on time-dependent deformation and failure behavior of rock samples, a triaxial creep test was conducted on gneiss after subjecting it to different number of F–T cycles. Then, the axial creep deformation and long-term strength of gneiss were analyzed and discussed. Additionally, the influence mechanism of F–T cycles on the creep mechanical behavior of gneiss was discussed using SEM techniques. Subsequently, based on the experimental results, a variable-parameter creep damage model that accounts for the effects of F–T cycles on gneiss was proposed. In the proposed model, the creep parameters of the rock gradually weakened with time, thereby reflecting the non-linear viscosity time-dependent characteristics of the rock. Using a variable-parameter creep damage model instead of a constant-parameter creep model was more accurate in predicting the time-dependent nonlinear deformation characteristics of the rock mass. The comparison between the creep test curve and fitting curve of the theoretical model verified the accuracy and applicability of the model.

Experimental procedure

Experimental apparatus

(1) Programmable Temperature

The appearance, control panel, and internal structure of the test equipment are shown in Fig. 1a, b. The device has a sinusoidal and linear (including constant temperature) regular compound programming capability, which is suitable for F–T cycles ranging from -70 to $150\ °C$ (freezing rock or soil). The digital screen displays the set temperature and actual temperature. The temperature uniformity is less than $2.0\ °C$, whereas the temperature deviation is within $\pm 2.0\ °C$.

(2) Testing system

The triaxial creep tests were performed on a rock servo-controlled triaxial equipment (Fig. 1c–e). The equipment included a loading system, constant-stability pressure equipment, hydraulic pressure transfer system, pressure chamber, hydraulic pressure system, and an automatic data collection system. The most important part of this equipment was the self-equilibrium triaxial pressure chamber system, which consisted of three high-precision pumps controlling the axial pressure, confining pressure, and pore water pressure. The maximum axial pressure, confining pressure, and pore water pressure was 2000 kN, 80 MPa, and 60 MPa, respectively. Additionally, the control precision was within $\pm 0.01\%$.

Rock specimen preparation

The rock samples that were not affected by F–T action were collected from the Huibai tunnel in the Jilin province in northeastern China. The rock surrounding the tunnel was primarily mixed gneiss. First, the entire rock block of the some tunnel face in the tunnel was transported to the laboratory from the site. Then, standard cylindrical specimens, which had a diameter of 50 mm and a height of 100 mm, were prepared, as shown in Fig. 2b, according to the standards proposed by the International Society for Rock Mechanics. The physical–mechanical parameters of the rock samples are listed in Table 1.

Experiment schedule

(1) F–T cycle test

The mechanical behavior of the surrounding rock in the entire F–T process has multi-field coupling characteristics, which is quite complex. Owing to the complexity of the problem, this study considers F–T cycle ($-20\ °C$ to $20\ °C$) as the external environmental conditions of the sample. In
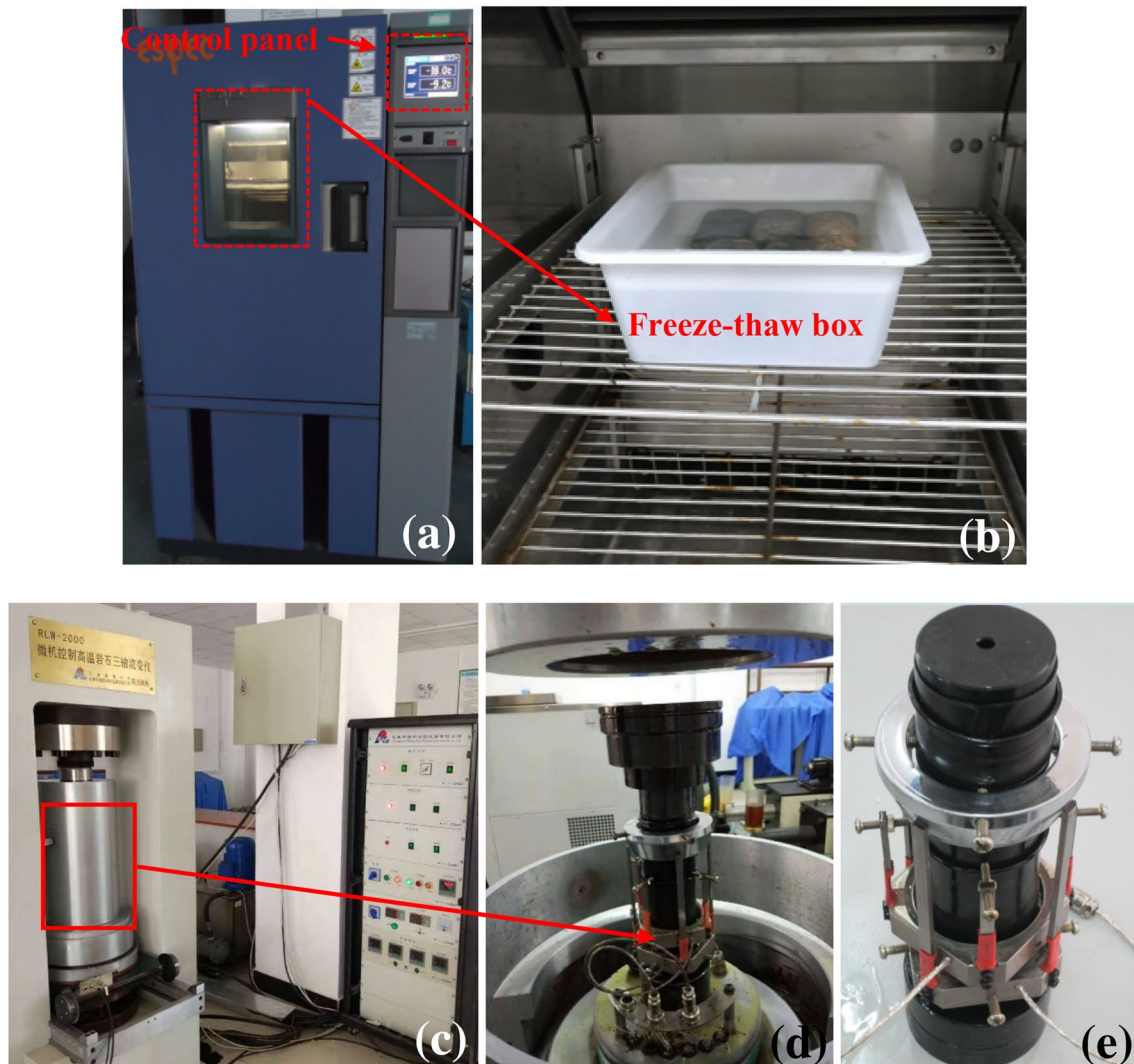
Fig. 1 Test equipment; **a** freezing–thawing device, **b** F–T box, **c** RLW-2000 rheological triaxial apparatus of rock, **d** pressure chamber, and **e** installed extensometer

other words, the indoor F–T cycle test simulates the F–T change of the surrounding rock at the tunnel entrance and the F–T temperature refers to the temperature change at the project site.

In the area where the Huibai Tunnel is located, the minimum and maximum temperatures in winter are − 20 °C and 22.4 °C, respectively. Therefore, the F–T cycle temperature range was determined to be − 20 °C to 20 °C. Two F–T cycles were calculated every day, and each cycle lasted for 12 h (6 h at − 20 °C and 6 h at 20 °C). The number of F–T cycles was set to 0, 20, 40, and 80, respectively. Three gneiss samples were prepared for each F–T cycle, i.e., there were 12 rock samples in total.

Before subjecting the samples to F–T cycles, they were saturated in a saturator for 6 h and then transferred into a container filled with water. Next, the samples were placed in a F–T box, where they remained saturated throughout the process.

(2) Triaxial compression creep test

Table 2 shows the triaxial compression creep test program of the rock sample. Based on the measured values of ground stress for tunnel engineering, the confining pressure was determined to be 5 MPa in the creep test. The axial load was applied at a constant rate of 0.5 MPa/min until the loading was stopped at a predetermined axial stress. The initial axial stress was 10 MPa, and the axial load $\Delta\sigma 1$ was applied progressively. During a multi-loading triaxial creep test, four to seven levels of axial stress were applied. The minimum holding time for each loading step was 24 h and the creep strain rate of the sample was less than 0.001 mm/h.
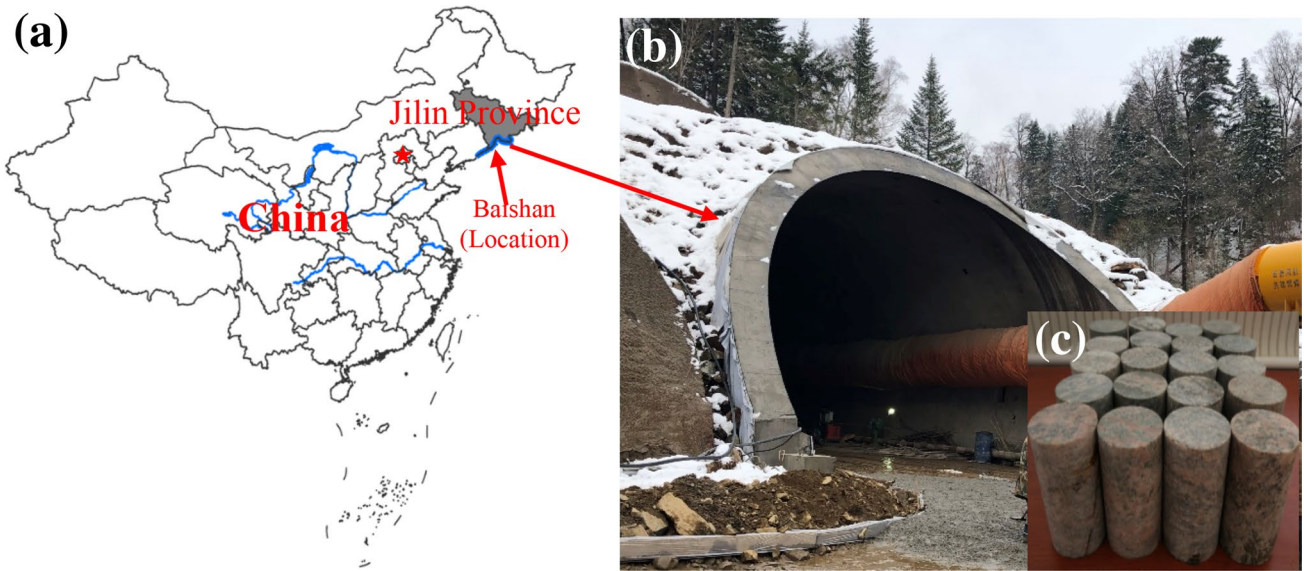
(3) Analysis of SEM images

Fig. 2 **a** Location of the study area; **b** Huibai tunnel entrance in winter; **c** standard specimens

Table 1 Physical–mechanical parameters of gneiss

Gneiss	Average density g/cm³	Porosity %	Uniaxial compressive strength MPa	Cohesion MPa	Elastic modulus GPa	Poisson's ratio
Mean	2.680	0.287	112.60	25.9	42.50	0.20

Table 2 Testing program of loading creep

Number	F–T cycles (N)	Temperature range (℃)	Confining pressure σ_3 (MPa)	Initial value σ_1 (MPa)	$\Delta\sigma$ (MPa)
G1	0	$-20\sim20$	5	10	20
G2	20				
G3	40				
G4	80				

To analyze the effect of F–T cycles on the mesostructure of gneiss, SEM was used to analyze the samples subjected to different number of F–T cycles by magnifying the SEM images up to 500 times.

Test results and analysis

Evolution of creep strain

The axial creep strain curves of gneiss obtained via the grading loading creep test for different number of F–T cycles are shown in Fig. 3. The instantaneous elastic strain occurs at the moment of stress application in gneiss samples,
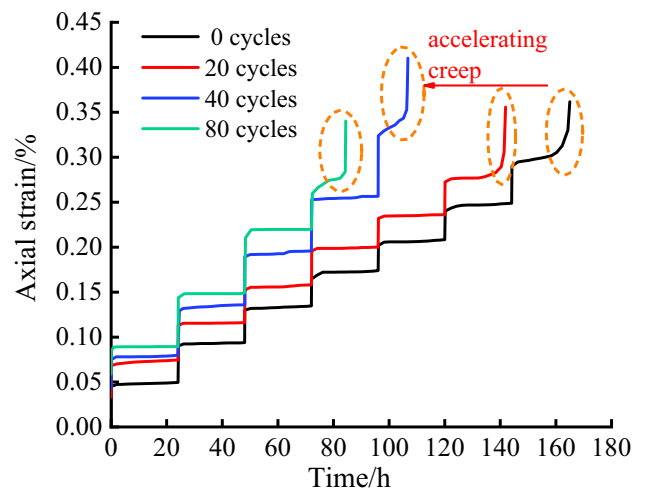

Fig. 3 Axial creep strain curves of samples subjected to different number of F–T cycles

whereas creep strain occurs under long-term stress. As the creep stress level increases, the slope of the creep curve increases gradually, and thereby shows the two stages of decelerating creep and steady-state creep. The creep rate eventually becomes constant with time. When the applied stress is sustained, the creep mechanical behavior of the

samples becomes increasingly obvious. Furthermore, when loading is at the last stage, the axial creep strain of the samples increases gradually with time, thereby experiencing the three-stage characteristics of rock creep, i.e., the decelerating creep stage, steady-state creep stage, and accelerated creep stage. Ultimately, the samples fail at the accelerated creep stage.

With the increase in the number of F–T cycles, the instantaneous elastic strain of the sample increases gradually at the same creep stress level although the creep duration and loading level decreases steadily. The more the number of F–T cycles, the more pores are generated inside the sample and more obvious the crack development. In the triaxial compression creep test, after the axial stress was applied, the micropores and microcracks in the sample closed gradually. This resulted in instantaneous elastic deformation, which increased with an increase in the number of F–T cycles. Simultaneously, the more the number of F–T cycles, the more obvious is the impact of the F–T cycles on the rock.

The axial creep strain of gneiss after being subjected to different number of F–T cycles at various axial stress levels is shown in Table 3. When the axial stress was 10 MPa, the initial instantaneous creep strain of the rock sample with 0 F–T cycles was 0.0467%. With an increase in the number of F–T cycles, the initial instantaneous creep strain of the rock samples subjected to 20, 40, and 80 F–T cycles increased by 49.50%, 60.56%, and 79.88%, respectively.

Additionally, the rock samples with 0 F–T cycles failed after 165.03 h, whereas the rock samples subjected to 20, 40, and 80 F–T cycles failed after 141.87 h, 106.75 h, and 84.42 h, respectively. Moreover, the loading level was reduced gradually from 7 to 6, 5, and 4. Therefore, at the same creep stress level, as the number of F–T cycles increased, the internal damage caused by freezing and thawing became larger and larger, resulting in an increase in the axial creep strain of the rock sample. However, the long-term strength and creep duration reduced as the loading level was reduced gradually.

As the number of F–T cycles increased, the F–T damage increased while the compressive strength of rock decreased along with the long-term strength. The main reasons for the internal F–T damage of the samples are mentioned below.

(1) Some of the water present in the microcracks of the saturated samples changed its phase and produced a frost heaving force. Therefore, when the temperature increases, the ice melts into water and enters the newly formed microcracks, resulting in the water continuously migrating from the unfrozen area to the frozen area. During the freezing process, additional frost heaving force is generated and the sample suffers the damage caused by the change in water–ice phase constantly.

(2) Because the expansion and contraction coefficients of mineral particles in the sample are not consistent, microcracks are produced due to the uneven deformation caused by F–T cycles, and thereby repeatedly subjected to the frost heaving force. After a certain number of cycles, the original cracks expand and generate new cracks.

To summarize, the water–ice phase change and uneven shrinkage and expansion of minerals in the samples during the F–T process leads to the expansion, convergence, and coalescence of microcracks, resulting in the F–T damage of rock samples and irreversible deterioration of mechanical properties. Therefore, the compressive strength, long-term strength, and elastic modulus decreased while creep strain deformation increased with an increase in the number of freeze–thaw cycles.

Creep strain rate analysis

Acceleration strain rate

The gneiss samples after being subjected to different F–T cycles entered creep failure in the creep failure stress level. The axial creep strain and creep strain rate of the gneiss samples under the creep failure stress level are shown in Fig. 4.

In the creep failure stress, the creep failure law is the same for all the samples, i.e., the decelerating creep stage develops into the accelerated creep stage via the steady-state creep stage. During the creep process, the decelerating creep stage and accelerated creep stage of the specimen lasted for a short period compared to the steady-state creep stage. Eventually, the samples failed in the accelerated creep stage.

Long-term strength

The long-term strength of rock mass is an important indicator of long-term stability and safety considering the time-dependent behavior (Damjanac and Fairhurst, 2010). The steady-state

Table 3 Axial creep strain of gneiss after different number of F–T cycles

Number	F–T cycles N	Axial creep strain under different axial stress (%)						
		10	30	50	70	90	110	130
G1	0	0.0497	0.0939	0.1346	0.1739	0.2083	0.2488	0.3618
G2	20	0.0743	0.1160	0.1581	0.1999	0.2362	0.3558	–
G3	40	0.0798	0.1359	0.1959	0.2566	0.4103	–	–
G4	80	0.0894	0.1490	0.2199	0.3404	–	–	–

(a) After 0 F-T cycles

(b) After 20 F-T cycles

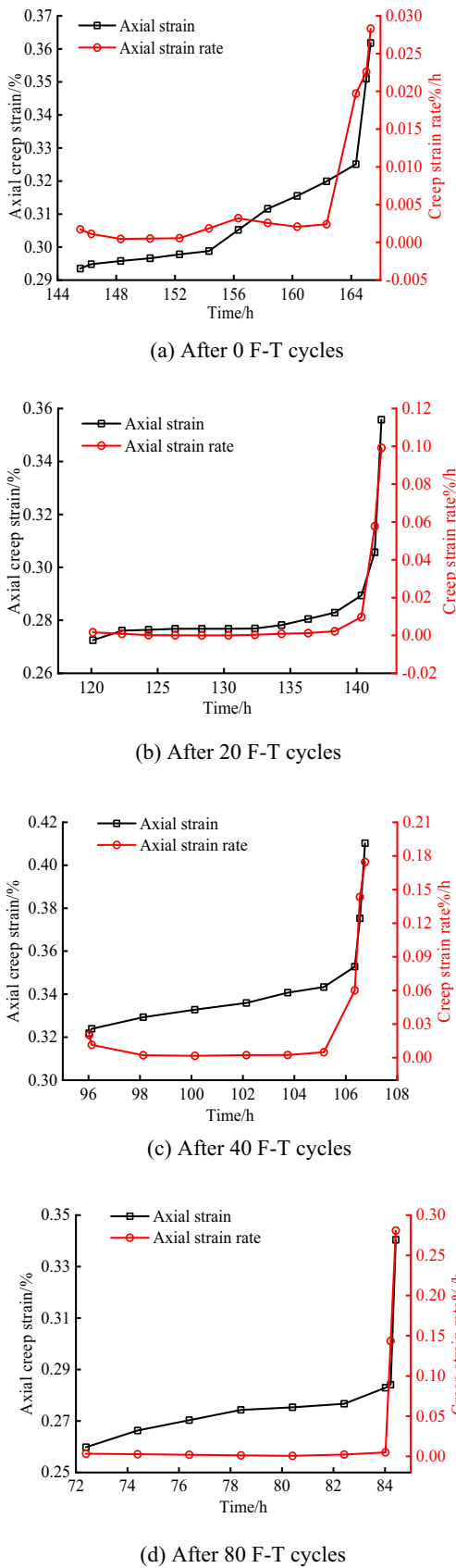(c) After 40 F-T cycles

(d) After 80 F-T cycles

Fig. 4 Axial creep strain and creep strain rate in the accelerated creep stage

creep rate method was used for data analysis in this study. Considering the G1 sample as an example, Fig. 5 shows the relationship between the stress and steady-state creep rate. There is a distinct inflection point on the curve. Moreover, the sections of the curve drawn before and after the inflection point intersect at point O. The stress corresponding to the intersection point O is the long-term strength of the rock.

The long-term strength of gneiss samples subjected to different F–T cycles is shown in Fig. 6. It can be observed that the long-term strength of the gneiss samples decreased gradually as the number of F–T cycles increased. The long-term strength of the rock sample after 0 F–T cycles was 123.8 MPa. Comparatively, the long-term strength of the rock samples decreased by 12.44%, 19.63%, and 32.80% after 20, 40, and 80 F–T cycles, respectively.

SEM analysis

The rock samples were analyzed using SEM to reveal the influence of F–T cycles on the microstructure of gneiss (Fig. 7).

Figure 7a illustrates that the surface of the rock sample after 0 F–T cycles had a compact flake structure with undeveloped joints. Furthermore, the surface was glossy and smooth, and the mineral particles were densely packed with few pores. As the number of F–T cycles increased, the thermal expansion and contraction between the mineral particles resulted in the loss of cement between the particles. Therefore, fragmentized mineral particles appeared, thereby developing pores and fissures (Fig. 7b–d).

As the number of F–T cycles increased, some of the cemented material was hydrolyzed under the influence of water–rock physical and chemical effects. The homogeneous mineral particles in the sample became loose, and the pores and micro-cracks in the sample continuously penetrated and expanded under the F–T effect to form cracks.

From the meso-damage characteristics of gneiss microcracks after freezing and thawing, it can be observed that the F–T cycles promoted surface development and internal damage of gneiss samples. First, when the rock was at subzero temperatures, the water in the cracks and pores froze into ice, which generated a frost heave force and caused frost damage to the rock. When the temperature increased, the ice in the rock melted into water, which migrated into secondary cracks and generated a large frost heave force in the rock during the freezing and thawing process. The ice-water phase change and water migration constantly deteriorated the rock damage. Additionally, the expansion coefficient and shrinkage coefficient of mineral particles in the sample were not consistent. During the F–T process, the sample deformed unevenly to generate cracks. Furthermore, the frost heaving force caused the cracks to develop continuously and generate secondary cracks, which caused friction

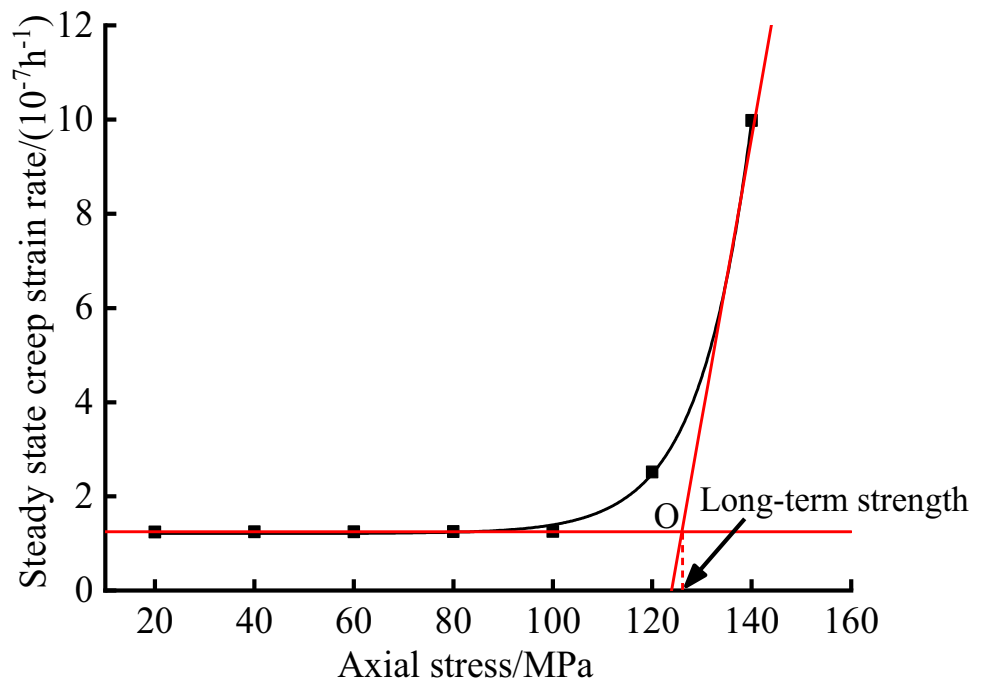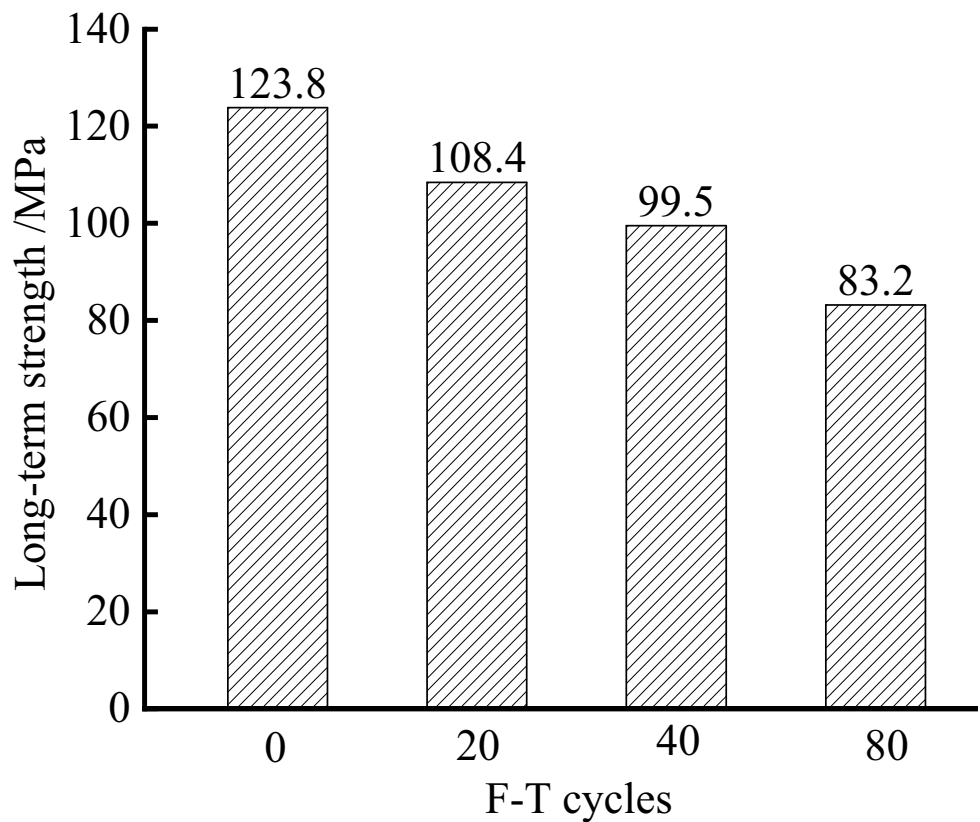**Fig. 5** Steady creep rate of gneiss under different stress levels ($N=0$)

Fig. 6 Long-term strength of gneiss after subjecting to different number of F–T cycles

between the particles and decreased the cementation force gradually. From a macro perspective, the main manifestation is the decrease in the cohesion of rock samples and compressive strength. This confirms that under the same creep stress level, the axial creep strain of the rock increases nonlinearly with the increase in the number of F–T cycles, whereas it is the opposite for the long-term strength ("Evolution of creep strain" and "Creep strain rate analysis").

(a) After 0 F-T cycles

(b) After 20 F-T cycles

(c) After 40F-T cycles
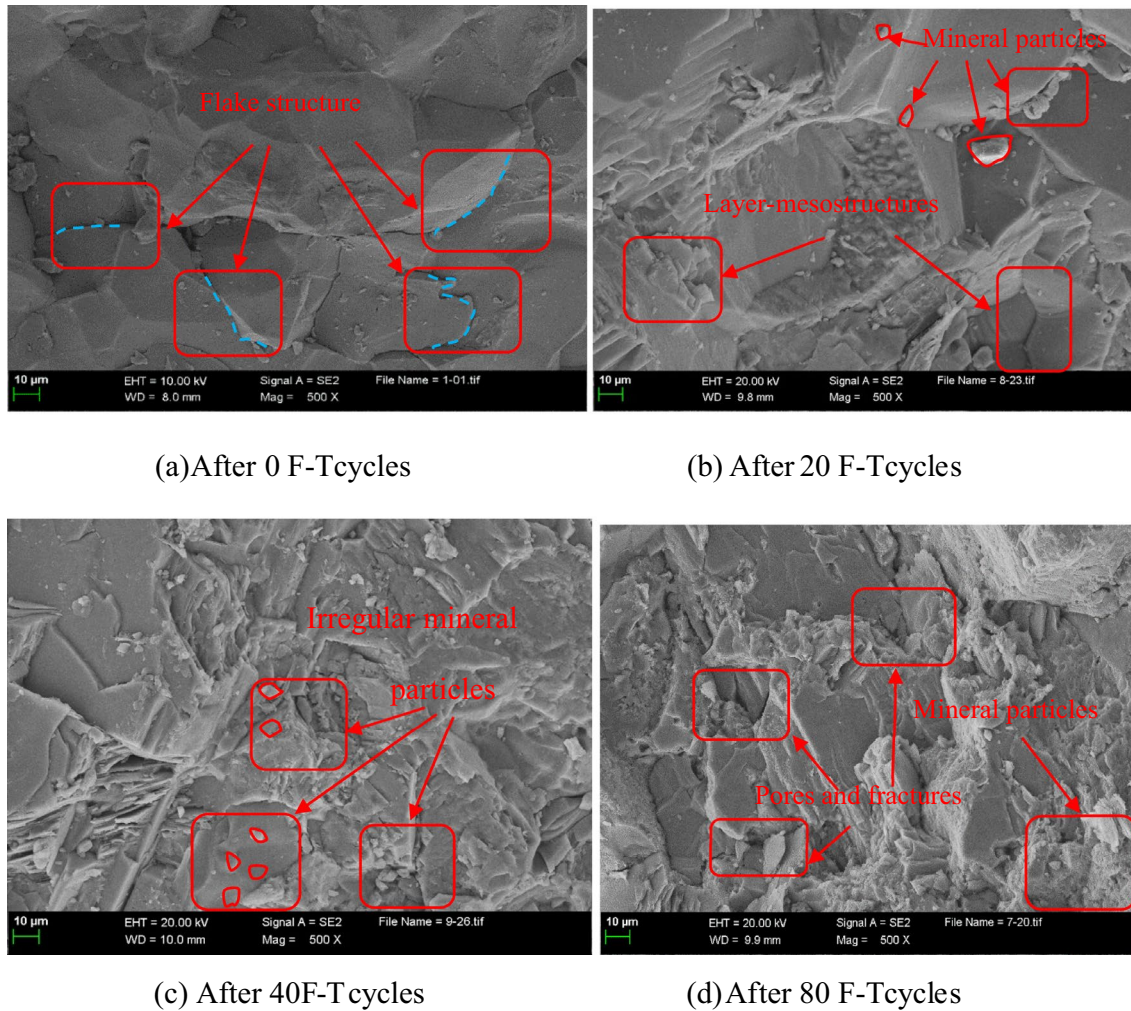
(d) After 80 F-T cycles

Fig. 7 Microscopic images of gneiss subjected to different number of F–T cycles

From the long-term stability perspective, the damage caused by F–T cycles affects the creep mechanical characteristics and parameters of the rock. Therefore, this phenomenon needs to be investigated further using the variable-parameter creep model.

Creep constitutive model of gneiss after F–T cycles

Unsteady creep parameters of gneiss after F–T cycles

The test results show that the gneiss sample fluctuated between hot and cold temperatures after being subjected to F–T cycles, resulting in thermal expansion and contraction and thereby deteriorating the mechanical properties of the rock. As the number of F–T cycles increased, the amount of creep deformation increased gradually, whereas the creep

rate increased significantly. However, the creep time, failure stress, and long-term strength reduced significantly. Therefore, treating the rheological parameters of rocks as unsteady will directly reflect the nonlinear aging characteristics of frozen and thawed rocks. This study considers the effect of the number of F–T cycles n on the gneiss elastic modulus E and viscosity coefficient η, i.e., $\eta E = En$ and $\eta = \eta n$, to derive the expression for unsteady creep parameters of frozen and thawed rocks.

Damaged viscous elements of rock after F–T cycles

When the applied load attains or exceeds a certain axial stress level, damage occurs inside the rock; therefore, the impact of the damage caused by the stress on the creep parameters should also be considered. The degree of damage in the decelerating creep stage and steady-state creep stage is relatively small. Therefore, this study only considers the damage caused by stress in the accelerated creep stage.

Owing to the various types of damage in the gneiss samples after the F–T cycles, the variable-parameter creep damage model should be used instead of the constant-parameter creep model to reflect the creep characteristics of the sample. In this study, the damage variable D was introduced to describe the damage deterioration of the viscosity coefficient of the sample during the accelerated creep stage. Furthermore, the influence of the number of F–T cycles n was considered. Therefore, the damaged viscous element under F–T conditions can be constructed, as shown in Fig. 8.

The constitutive relationship of damaged viscous elements after F–T cycles is given by:

$$\sigma = \eta(n, D)\dot{\varepsilon} \tag{1}$$

where σ and $\dot{\varepsilon}$ are the stress and creep strain rate of the viscous elements damaged by F–T cycles, respectively, and $\eta(n, D)$ is the viscous coefficient of the viscous elements damaged by the F–T cycles. Considering the effects of F–T cycles and stress on the viscosity coefficient, the viscous coefficient of the visco-damage elements can be written as:

$$\eta(n, D) = \eta(n)(1 - D) \tag{2}$$

where $\eta(n)$ is the viscosity coefficient of the samples after n F–T cycles and D is the damage variable, $0 \leq D < 1$.

In the rock creep process, the damage variable has a negative exponential function of time, as shown in Eq. (3).
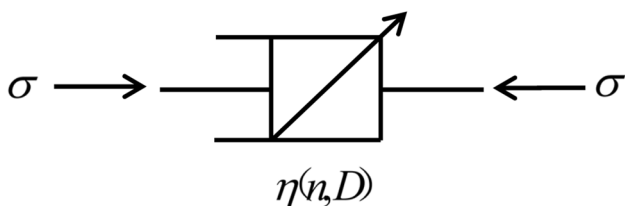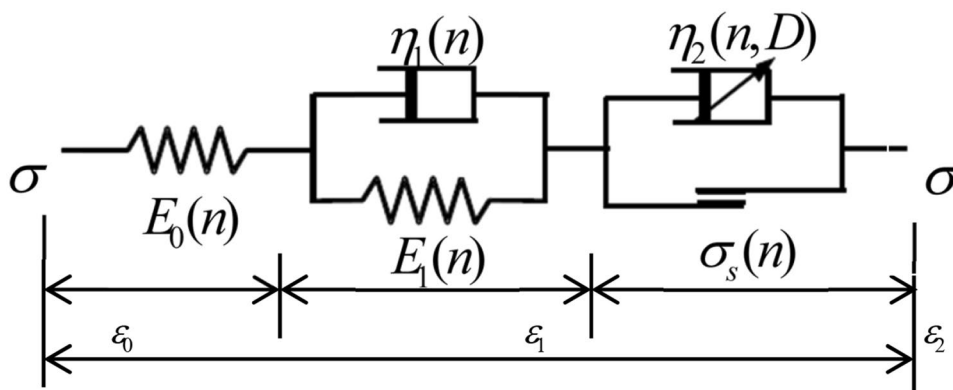

$\sigma \longrightarrow$ $\longleftarrow \sigma$

$\eta(n, D)$

Fig. 8 Damaged viscous element of gneiss after F–T cycles

Fig. 9 Creep constitutive model of gneiss after F–T cycles

$\eta_1(n)$ $\eta_2(n, D)$

σ $E_0(n)$ $E_1(n)$ $\sigma_s(n)$ σ

ε_0 ε_1 ε_2

$$D = 1 - e^{-\alpha t} \tag{3}$$

where α is the coefficient related to the number of F–T cycles n and t is the creep time. Therefore, the viscosity coefficient of the damaged viscous components is shown in Eq. (4).

$$\eta(n, D) = \eta(n)e^{-\alpha(n)t} \tag{4}$$

By maintaining the stress constant and combining Eq. (1) and Eq. (4), the constitutive relationship of the damaged viscous element of gneiss after the F–T cycles is shown in Eq. (5).

$$\varepsilon(t) = \frac{\sigma}{\alpha(n)\eta(n)}\left[e^{\alpha(n)t} - 1\right] \tag{5}$$

Variable-parameter creep damage model

The experiments showed that the gneiss samples experienced the decelerating creep stage, steady-state creep stage, and accelerated creep stage after the F–T cycles. In the creep tests, the classic Nishihara model can describe the deceleration creep and steady-state creep stages, but it cannot reflect the accelerated creep stage characteristics of rocks. Therefore, based on the Nishihara model, the viscous elements in the viscoplastic body were replaced by F–T-damaged viscous elements, and the effect of F–T cycles on the model parameters was considered to establish the creep constitutive model of gneiss after the F–T cycles, as shown in Fig. 9. This model was composed of an F–T elastic body, F–T viscoelastic body, and F–T-damaged viscoplastic body and the strains were ε_0, ε_1 and ε_2, respectively.

When the axial stress was σ, the total strain ε was given, as shown in Eq. (6).

$$\varepsilon = \varepsilon_0 + \varepsilon_1 + \varepsilon_2 \tag{6}$$

For the F–T elastic elements, the stress–strain relationship was given using Eq. (7).

$$\varepsilon_0 = \frac{\sigma}{E_0(n)} \tag{7}$$

where $E_0(n)$ is the elastic modulus of the elastic element after n F–T cycles.

The F–T viscoelastic elements were composed of an F–T elastic element and an F–T viscous element in parallel. For the F–T viscous element, the constitutive relationship was given by:

$$\sigma_v = \eta_1(n)\dot{\varepsilon}_v \tag{8}$$

where, σ_v, $\dot{\varepsilon}_v$ and $\eta_1 n$ are the stress, strain rate, and viscosity coefficients of the viscous element in the F–T viscoelastic body, respectively.

Therefore, according to the combined model theory, the stress–strain relationship of the F–T viscoelastic body is given by:

$$\begin{cases} \varepsilon_1 = \varepsilon_e = \varepsilon_v \\ \sigma = \sigma_e + \sigma_v = E_1(n)\varepsilon_e + \eta_1(n)\dot{\varepsilon}_v \end{cases} \tag{9}$$

where ε_e and $E_1(n)$ are the elastic strain and elastic modulus of the elastic element in the F–T viscoelastic body, respectively. By combining with the initial condition $t=0$, Eq. (9) can be solved, as shown in Eq. (10).

$$\varepsilon_1 = \frac{\sigma}{E_1(n)}\left(1 - e^{-\frac{E_1(n)}{\eta_1 n}t}\right) \tag{10}$$

The F–T-damaged viscoplastic elements were composed of F–T-damaged viscous elements and plastic elements. The stress of the plastic element can be expressed using Eq. (11).

$$\sigma_p = \begin{cases} \sigma, \sigma < \sigma_s \\ \sigma_s, \sigma \geq \sigma_s \end{cases} \tag{11}$$

where σ_s is the yield stress.

The total stress of the F–T damage viscoplastic elements is given using Eq. (12).

$$\sigma = \sigma_v + \sigma_p \tag{12}$$

where σ_v is the stress of the F–T-damaged viscous elements.

If $\sigma < \sigma_s$, combining Eq. (11) and (12) provides $\sigma_v = 0$, i.e., $\eta_2 = 0$.

If $\sigma\sigma_s$, then,

$$\eta_2 = \frac{\sigma}{\alpha(n)\eta_2(n)}\left[e^{\alpha(n)t} - 1\right] \tag{13}$$

Therefore, the stress–strain relationship of F–T-damaged viscoplastic elements is given using Eq. (14).

$$\varepsilon_2 = \begin{cases} 0, \sigma < \sigma_s \\ \dfrac{\sigma - \sigma_s}{\alpha(n)\eta_2(n)}\left[e^{\alpha(n)t} - 1\right]\sigma \geq \sigma_s \end{cases} \tag{14}$$

Considering the strains of the F–T elastic body, F–T viscoelastic body, and F–T-damaged viscoplastic body, the one-dimensional constitutive equation of gneiss samples for the F–T creep model can be expressed using Eq. (15).

$$\varepsilon(t) = \begin{cases} \dfrac{\sigma}{E_0(n)} + \dfrac{\sigma}{E_1(n)}\left(1 - e^{-\frac{E_1(n)}{\eta_1 n}t}\right), (\sigma > \sigma_s) \\ \dfrac{\sigma}{E_0(n)} + \dfrac{\sigma}{E_1(n)}\left(1 - e^{-\frac{E_1(n)}{\eta_1 n}t}\right) + \dfrac{\sigma - \sigma_s}{\alpha(n)\eta_2(n)}\left[e^{\alpha(n)t} - 1\right], (\sigma \geq \sigma_s) \end{cases} \tag{15}$$

In the three-dimensional stress state, assuming that the total strain of the viscoelastic-plastic damage creep model is ε_{ij}, strain of the elastic body is ε_{ij}^e, strain of the viscoelastic body is ε_{ij}^{ve}, and strain of the damaged viscoplastic body is ε_{ij}^{vp}. Therefore, according to the superposition principle, the total strain can be obtained using Eq. (16).

$$\varepsilon_{ij} = \varepsilon_{ij}^e + \varepsilon_{ij}^{ve} + \varepsilon_{ij}^{vp}$$

For an elastic body, the stress tensor σ_{ij} at any point in the rock under a three-dimensional stress state can be divided into a spherical stress tensor $\sigma_m\delta_{ij}$ and deviatoric stress tensor S_{ij}. Similarly, the strain tensor ε_{ij} at any point in the interior can be divided into a spherical strain tensor $\varepsilon_m\delta_{ij}$ and deviatoric strain tensor e_{ij}.

$$\left.\begin{aligned} \sigma_{ij} &= \sigma_m\delta_{ij} + S_{ij} \\ \varepsilon_{ij} &= \varepsilon_m\delta_{ij} + e_{ij} \end{aligned}\right\} \tag{17}$$

where δ_{ij} is Kronecker symbol.

According to Hooke's law, we obtain:

$$\left.\begin{aligned} \sigma_m &= 3K_0\varepsilon_m \\ S_{ij} &= 2G_0 e_{ij} \end{aligned}\right\} \tag{18}$$

Consequently, the three-dimensional creep equation of the elastic body can be expressed as follows:

$$\varepsilon_{ij}^e = \frac{S_{ij}}{2G_0(n)} + \frac{\sigma_m\delta_{ij}}{3K_0(n)} \tag{19}$$

where $K_0(n)$ and $G_0(n)$ are the bulk modulus and shear modulus of the F–T elastic body, respectively.

The three-dimensional creep equation of the viscoelasticity body can be expressed as follows:

$$\varepsilon_{ij}^{ve} = \frac{S_{ij}}{2G_1(n)}\left[1 - \exp\left(-\frac{G_1(n)}{\eta_1(n)}t\right)\right] \tag{20}$$

where $G_1(n)$ and $\eta_1(n)$ are the shear modulus and viscosity coefficient of the F–T viscoelastic body, respectively.

The three-dimensional creep equation of the F–T-damaged viscoplastic body can be expressed as follows:

$$\varepsilon = \begin{cases} \dfrac{S_{ij}}{2G_0(n)} + \dfrac{\sigma_m \delta_{ij}}{3K_0(n)} + \dfrac{S_{ij}}{2G_1(n)}\left[1 - \exp\left(-\dfrac{G_1(n)}{\eta_1(n)}t\right)\right] & (F < 0) \\[2ex] \dfrac{S_{ij}}{2G_0(n)} + \dfrac{\sigma_m \delta_{ij}}{3K_0(n)} + \dfrac{S_{ij}}{2G_1(n)}\left[1 - \exp\left(-\dfrac{G_1(n)}{\eta_1(n)}t\right)\right] + \dfrac{e^{\alpha(n)t}-1}{\alpha(n)\eta_2(n)}\left(\dfrac{F}{F_0}\right)\dfrac{\partial F}{\partial \sigma_{ij}} & (F \geq 0) \end{cases} \tag{23}$$

$$\varepsilon_{ij}^{vp} = \frac{1}{\alpha(n)\eta_2(n)}\left\langle \phi\left(\frac{F}{F_0}\right)\right\rangle \frac{\partial Q}{\partial \sigma_{ij}} t \tag{21}$$

where $\left\langle \phi\left(\dfrac{F}{F_0}\right)\right\rangle$ is the switch function, which is written as:

$$\left\langle \phi\left(\frac{F}{F_0}\right)\right\rangle = \begin{cases} 0 & (F < 0) \\ \phi\left(\dfrac{F}{F_0}\right) & (F \geq 0) \end{cases} \tag{22}$$

where F is the rock yield function and F_0 is the initial value of the rock yield function. $\phi\left(\dfrac{F}{F_0}\right)$ is a power function, i.e., $\phi\left(\dfrac{F}{F_0}\right) = \left(\dfrac{F}{F_0}\right)^k$, where k is the specified constant, which is generally 1 (Abu Al-Rub et al. 2013), and Q is the plastic potential function. Additionally, for the convenience of

calculation, the associated flow rule was adopted for the plastic flow, i.e., $F = Q$ (Moghadam et al. 2013).

According to Eqs. (15), (19), (20), and (21), the creep equation of F–T-damaged rock in the three-dimensional state can therefore be expressed as shown in Eq. (23).

Verification and parameter analysis of the constitutive model

Adopt the Boltzmann superposition principle to process the creep curve. Based on the experimental results, the mathematical optimization analysis software 1stOpt was used to identify the model parameters. The creep parameter identification results of gneiss samples under the creep failure stress after undergoing 0, 20, 40, and 80 F–T cycles are shown in Table 4.

Figure 10 shows the comparison between the creep test curve and fitting curve of the theoretical model under the creep failure stress after 0, 20, 40, and 80 F–T cycles of the samples. The model fitting curve reflects the

Table 4 Creep model parameters of gneiss considering F–T damage

F–T cycles (n)	Axial stress (MPa)	E_0 (GPa)	E_1 (GPa)	η_1 (GPa·h)	η_2 (GPa·h)	α
0	10	458.89	206.83	96.21	–	–
	30	447.78	112.38	61.84	–	–
	50	445.76	100.49	41.02	–	–
	70	426.20	82.15	12.70	–	–
	90	382.31	20.06	8.31	–	–
	110	332.09	17.96	4.84	–	–
	130	151.55	14.64	1.46	2942.86	0.43
20	10	434.67	141.77	61.19	–	–
	30	367.39	110.66	51.71	–	–
	50	318.01	72.14	29.42	–	–
	70	286.52	36.70	10.13	–	–
	90	262.11	18.24	7.12	–	–
	110	226.25	12.11	2.93	2556.46	0.59
40	10	358.48	113.63	52.93	–	–
	30	303.80	90.91	31.01	–	–
	50	282.65	53.78	26.36	–	–
	70	255.29	26.10	8.33	–	–
	90	248.74	14.71	3.07	2336.02	0.71
80	10	312.80	87.28	37.02	–	–
	30	286.11	79.42	27.68	–	–
	50	250.99	27.37	12.65	–	–
	70	209.77	14.01	3.19	2286.90	0.92

(a) After 0 F-T cycles

(b) After 20 F-T cycles

(c) After 40 F-T cycles
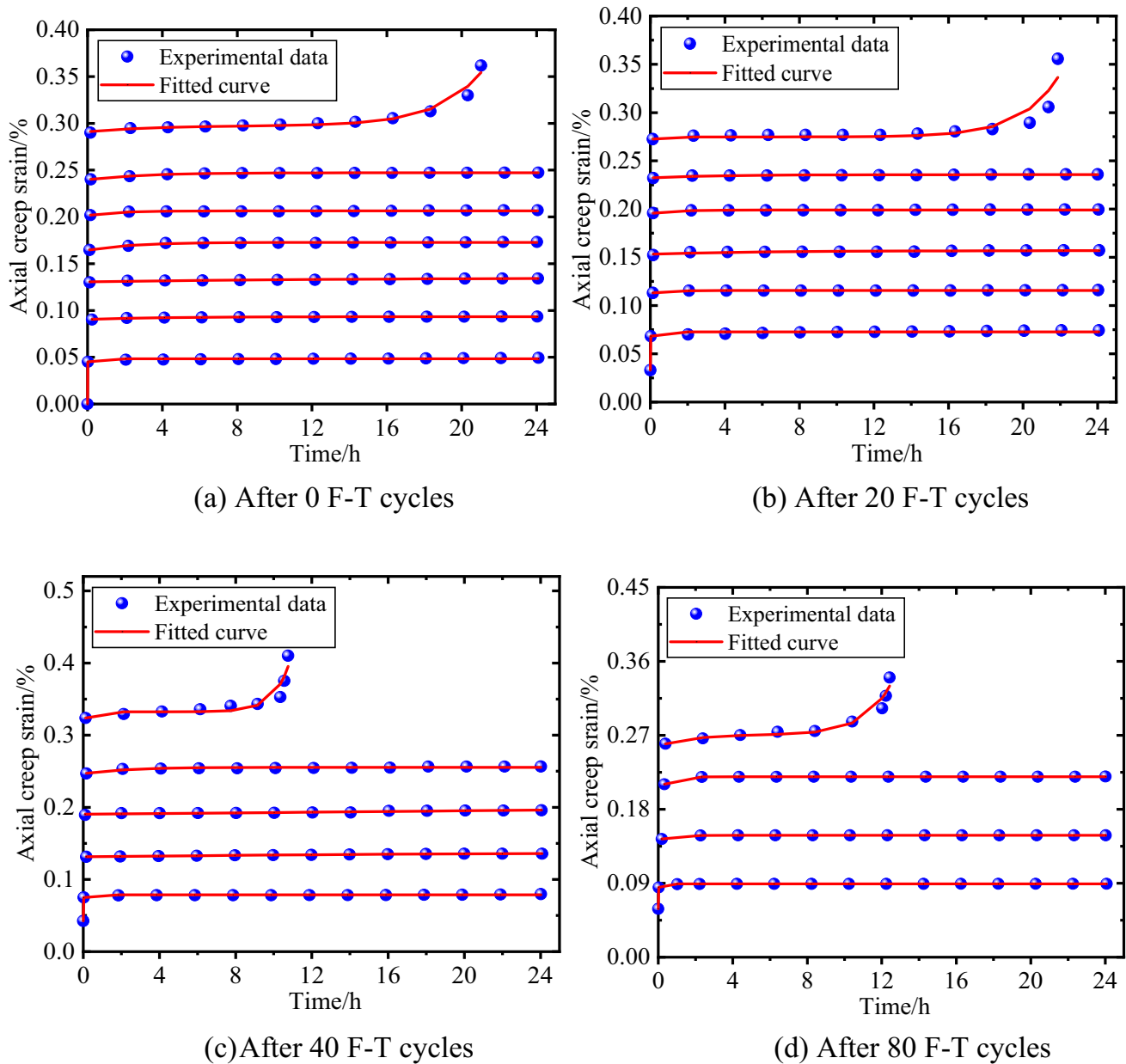

(d) After 80 F-T cycles

Fig. 10 Comparisons of test curve and theoretical model fitting curve

characteristics of decelerating creep, steady-state creep, and accelerated creep stage under different F–T cycles. This verifies the accuracy and applicability of the F–T-damaged creep constitutive model established in this study.

Furthermore, this section analyzes the sensitivity of creep parameters η_2 and α of viscous elements damaged by freezing and thawing of rocks and investigates their influence on the creep deformation of gneiss. For other creep parameters, the values listed in Table 4 under the last stage load of 80 F–T cycles were selected.

Figures 11 and 12 show the effect of changes in creep parameters η_2 and α on creep deformation, respectively. Figure 11 indicates that when other parameters remain unchanged, the steady-state creep rate and creep deformation of the rock decreases gradually, whereas the steady-state creep time increases as the viscosity coefficient η_2 increases. Figure 12 shows that with the increase in the creep parameter α, the creep rate and creep deformation of the accelerated creep stage increased gradually as the creep failure time decreased. Then, the rock transitioned from viscoelastic to viscoelastic-plastic.

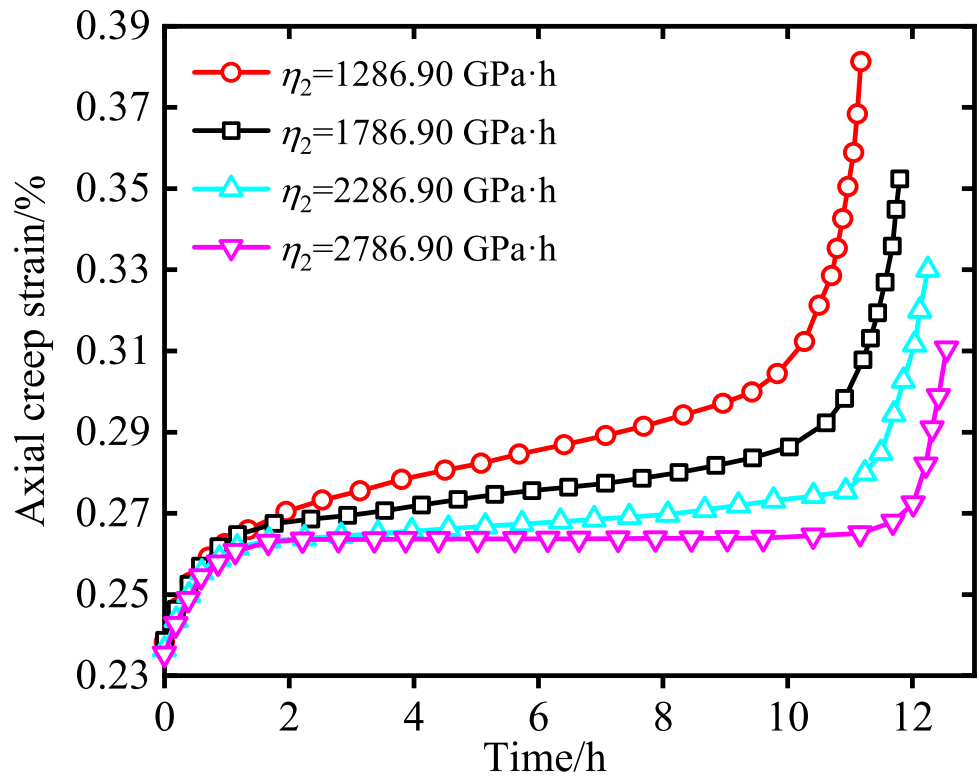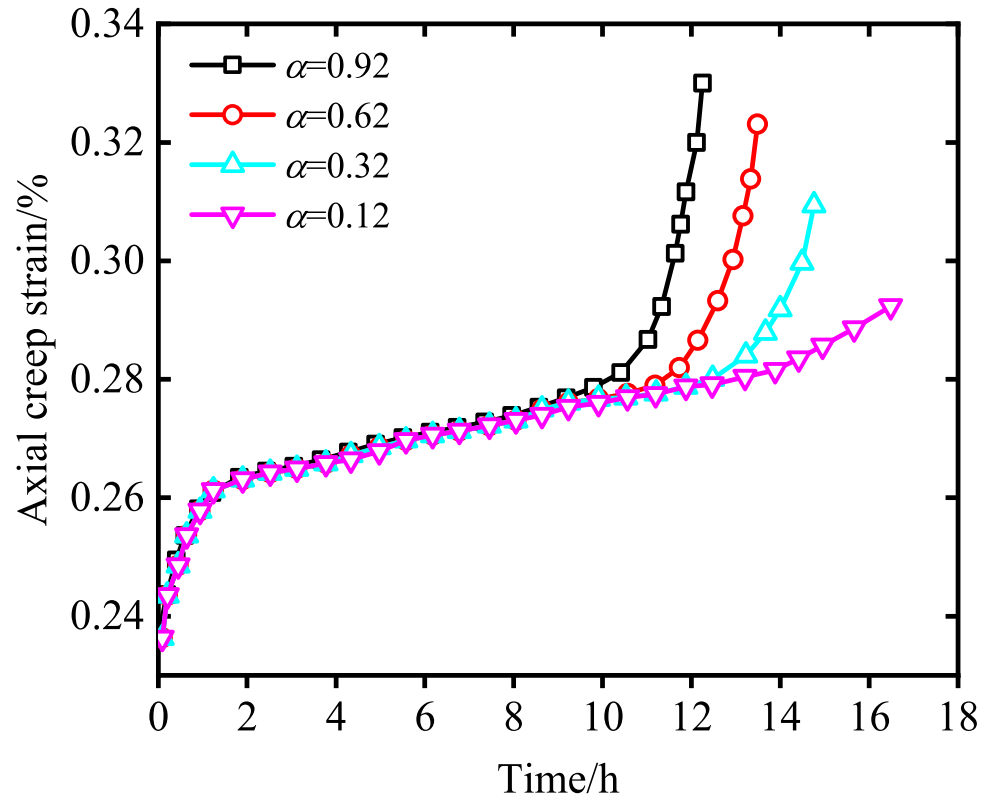**Fig. 11** Effect of creep parameter η_2 on the creep curve

Fig. 12 Effect of creep parameter α on the creep curve

Variation of creep model parameters with respect to F–T cycles

According to the fitting results between the creep model parameters and F–T cycles shown in Table 1, each creep parameter was averaged under the same F–T cycle, and the relationship between the creep parameters and F–T cycles is shown in Eq. (24).

$$
\left.
\begin{aligned}
E_0(n) &= 118.97e^{-0.035n} + 258.459, R^2 = 0.9967 \\
E_1(n) &= 29.78e^{-0.028n} + 49.226, R^2 = 0.9952 \\
\eta_1(n) &= 15.39e^{-0.019n} + 16.862, R^2 = 0.9976 \\
\eta_2(n) &= 692.32e^{-0.0453n} + 2254.619, R^2 = 0.9864 \\
\alpha(n) &= 0.006n + 0.452, R^2 = 0.9900
\end{aligned}
\right\}
\quad (24)
$$

The fitting curve of each parameter of the creep model with respect to the number of F–T cycles n is shown in Fig. 13. As per the exponential function, the elastic moduli (E_0 and E_1) and viscosity coefficient (η_1 and η_2) decreased gradually with the increase in the number of F–T cycles. The relationship between the correlation coefficient α and the number of F–T cycles is linear, and the value of α increases with the increase in the number of F–T cycles. Additionally, the changes in the model parameters causes the creep deformation and creep rate to increase gradually with the increase in the number of F–T cycles, and this is consistent with the experimental results.

Discussion

During the F–T cycles, the micro-cracks inside the gneiss expand, collect, and interpenetrate, thereby affecting the creep mechanical behavior of the rock and threatening the long-term stability of rock engineering. The aforementioned characteristics were only analyzed for creep, long-term strength, and microscopic morphology of the rock after the F–T cycles.
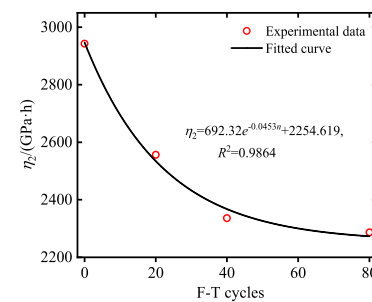
1. As the number of F–T cycles increased, water migration and aggregation caused frost heaving damages to the rock mass. Additionally, the expansion of frost heaving cracks intensified gradually with time. Because of the formation of frost heaving force due to F–T cycles, the cracks expand to produce secondary cracks and new cracks, which decrease the friction between the skeleton particles and cement. Consequently, as the number of F–T cycles increases, the long-term strength of the rock sample decreases. This confirms that under the same creep stress level, the axial creep strain of the rock
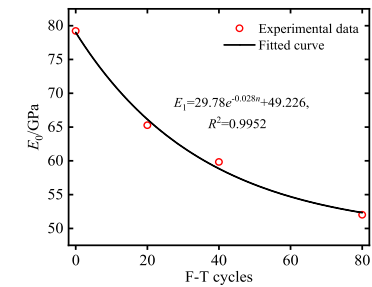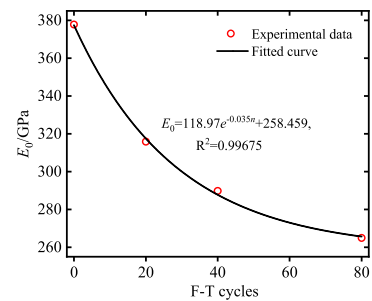
(b) Fitting curve of E_1 with respect to F-T cycles n
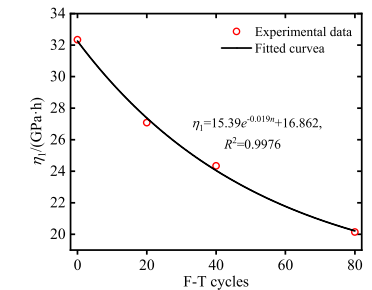
(c) Fitting curve of η_1 with respect to F-T cycles n

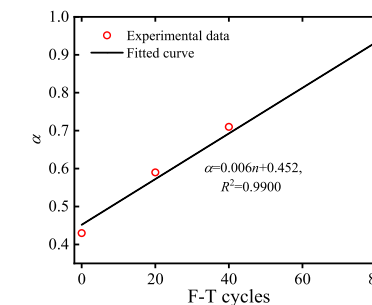(d) Fitting curve of η_2 with respect to F-T cycles n

Fig. 13 Variation curve of creep parameters with respect to F–T cycles

increases nonlinearly with the increase in the number of F–T cycles (Sect. Evolution of creep strain)

2. The expansion coefficients of the rock mineral particles are different. Therefore, when the F–T temperature ranges are different, the effect of F–T cycles on the creep mechanical properties of rocks is also different. The effect of F–T temperature range on the experimental results and creep model were not analyzed in depth. Hence, this will be our next research emphasis.

3. In tunnel construction in cold regions, the mechanical behavior of the surrounding rock of the tunnel during the entire process of freezing and thawing has multi-field coupling characteristics, which is quite complicated. Therefore, this study considers F–T cycles as an environmental condition for rocks. The creep test and F–T cycle test were detached, i.e., the rock was first subjected to F–T treatment and then the creep mechanical behavior of the sample was studied. However, the actual surrounding rock deformation problem of tunnels in the cold region includes the time-dependent behavior of the rock under the F–T cycle. Furthermore, there are superposition problems of frost heave deformation and creep deformation of the rock under freezing and thawing. However, this was not investigated in this study. Therefore, the authors will further study this topic by analyzing the creep mechanical behavior of rocks while freezing and thawing and in the frozen state.

Conclusion

In this study, the results of the triaxial creep test and the creep constitutive damage model for gneiss were analyzed after subjecting the Huibai tunnel rock samples to F–T cycles. The following conclusions were obtained.

1. The number of F–T cycles has a significant effect on the creep mechanical behavior of gneiss. The creep deformation increased gradually with the increase in the number of F–T cycles. However, the creep failure stress, creep duration, and long-term strength showed a decreasing trend.

2. The influence mechanism of F–T cycles on the microscopic structure of gneiss was explained using SEM analysis. As the number of F–T cycles increased, some of the cemented material in gneiss hydrolyzed under the influence of water–rock physical and chemical effects. This loosened the homogeneous mineral particles, and the pores and micro-cracks penetrated continuously and expanded to form cracks.

3. Based on the experimental results, a variable-parameter creep damage model was proposed considering the

effect of F–T cycles on gneiss. The creep-damage model was composed of three components: a Hooke body, a Kelvin body (parallel viscoelastic components), and a new nonlinear viscoplastic damage component. The creep-damage model not only describes the three typical creep stages (primary creep, secondary creep, and tertiary creep), but also reflects the effect of F–T damage on the creep failure stress. The comparison between the creep test curve and fitting curve of the theoretical model verified the accuracy and applicability of the model.

References

Abu Al-Rub RK, Darabi MK, Kim S-M, Little DN, Glover CJ (2013) Mechanistic-based constitutive modeling of oxidative aging in aging-susceptible materials and its effect on the damage potential of asphalt concrete. Constr Build Mater 41:439–454. https://doi.org/10.1016/j.conbuildmat.2012.12.044

Bayram F (2012) Predicting mechanical strength loss of natural stones after freeze-thaw in cold regions. Cold Reg Sci Technol 83–84:98–102. https://doi.org/10.1016/j.coldregions.2012.07.003

Chen TC, Yeung MR, Mori N (2004) Effect of water saturation on deterioration of welded tuff due to freeze-thaw action. Cold Reg Sci Technol 38:127–136. https://doi.org/10.1016/j.coldregions.2003.10.001

Damjanac B, Fairhurst C (2010) Evidence for a long-term strength threshold in crystalline rock. Rock Mech Rock Eng 43:513–531. https://doi.org/10.1007/s00603-010-0090-9

de Argandona VGR, Rey AR, Celorio C, del Rio LMS, Calleja L, Llavona J (1999) Characterization by computed X-ray tomography of the evolution of the pore structure of a dolomite rock during freeze-thaw cyclic tests. Phys Chem Earth Part A Sol Earth and Geodesy 24:633–637. https://doi.org/10.1016/s1464-1895(99)00092-7

Grossi CM, Brimblecombe P, Harris I (2007) Predicting long term freeze-thaw risks on Europe built heritage and archaeological sites in a changing climate. Sci Total Environ 377:273–281. https://doi.org/10.1016/j.scitotenv.2007.02.014

Hamza O, Stace R (2018) Creep properties of intact and fractured muddy siltstone. Int J Rock Mech Min Sci 106:109–116. https://doi.org/10.1016/j.ijrmms.2018.03.006

Hou R, Zhang K, Tao J, Xue X, Chen Y (2019) A nonlinear creep damage coupled model for rock considering the effect of initial damage. Rock Mech Rock Eng 52:1275–1285. https://doi.org/10.1007/s00603-018-1626-7

Hu B, Yang S-Q, Xu P, Cheng J-L (2019) Cyclic loading-unloading creep behavior of composite layered specimens. Acta Geophys 67:449–464. https://doi.org/10.1007/s11600-019-00261-x

Jamshidi A, Nikudel MR, Khamehchiyan M (2013) Predicting the long-term durability of building stones against freeze-thaw using a decay function model. Cold Reg Sci Technol 92:29–36. https://doi.org/10.1016/j.coldregions.2013.03.007

Karaca Z, Deliormanli AH, Elci H, Pamukcu C (2010) Effect of freeze-thaw process on the abrasion loss value of stones. Int J Rock Mech Min Sci 47:1207–1211. https://doi.org/10.1016/j.ijrmms.2010.07.003

Ke B, Zhou K, Xu C, Deng H, Li J, Bin F (2018) Dynamic mechanical property deterioration model of sandstone caused by freeze-thaw weathering. Rock Mech Rock Eng 51:2791–2804. https://doi.org/10.1007/s00603-018-1495-0

Khanlari G, Sahamieh RZ, Abdilor Y (2015) The effect of freeze-thaw cycles on physical and mechanical properties of Upper Red Formation sandstones, central part of Iran. Arab J Geosci 8:5991–6001. https://doi.org/10.1007/s12517-014-1653-y

Lai YM, Hui W, Wu ZW, Liu SY, Den XJ (2000) Analytical viscoelastic solution for frost force in cold-region tunnels. Cold Reg Sci Technol 31:227–234. https://doi.org/10.1016/s0165-232x(00)00017-3

Lin Z, Niu F, Li X, Li A, Liu M, Luo J, Shao Z (2018) Characteristics and controlling factors of frost heave in high-speed railway subgrade, Northwest China. Cold Reg Sci Technol 153:33–44. https://doi.org/10.1016/j.coldregions.2018.05.001

Liu B, Ma Y, Zhang G, Xu W (2018) Acoustic emission investigation of hydraulic and mechanical characteristics of muddy sandstone experienced one freeze-thaw cycle. Cold Reg Sci Technol 151:335–344. https://doi.org/10.1016/j.coldregions.2018.03.029

Liu B, Ma Y, Liu N, Han Y, Li D, Deng H (2019) Investigation of pore structure changes in Mesozoic water-rich sandstone induced by freeze-thaw process under different confining pressures using digital rock technology. Cold Reg Sci Technol 161:137–149. https://doi.org/10.1016/j.coldregions.2019.03.006

Liu H, Yuan X, Xie T (2019) A damage model for frost heaving pressure in circular rock tunnel under freezing-thawing cycles. Tunn Undergr Space Technol 83:401–408. https://doi.org/10.1016/j.tust.2018.10.012

Ma JZ, Zhang J, Huang HW, Zhang LL, Huang JS (2017) Identification of representative slip surfaces for reliability analysis of soil slopes based on shear strength reduction. Comput Geotech 85:199–206. https://doi.org/10.1016/j.compgeo.2016.12.033

Matsuoka N (1990) Mechanisms of rock breakdown by frost action—an experimental approach. Cold Reg Sci Technol 17:253–270. https://doi.org/10.1016/s0165-232x(05)80005-9

Moghadam SN, Mirzabozorg H, Noorzad A (2013) Modeling time-dependent behavior of gas caverns in rock salt considering creep, dilatancy and failure. Tunn Undergr Space Technol 33:171–185. https://doi.org/10.1016/j.tust.2012.10.001

Mutluturk M, Altindag R, Turk G (2004) A decay function model for the integrity loss of rock when subjected to recurrent cycles of freezing-thawing and heating-cooling. Int J Rock Mech Min Sci 41:237–244. https://doi.org/10.1016/s1365-1609(03)00095-9

Park J, Hyun C-U, Park H-D (2015) Changes in microstructure and physical properties of rocks caused by artificial freeze-thaw action. Bull Eng Geol Env 74:555–565. https://doi.org/10.1007/s10064-014-0630-8

Qiangyong Z, Wendong Y, Jianguo Z, Chunhe Y (2009) Variable parameters-based creep damage consitutive model and its engineering application. Chin J Rock Mechan Eng 28:732–739

Rassouli FS, Zoback MD (2018) Comparison of short-term and long-term creep experiments in shales and carbonates from unconventional gas reservoirs. Rock Mech Rock Eng 51:1995–2014. https://doi.org/10.1007/s00603-018-1444-y

Takarli M, Prince W, Siddique R (2008) Damage in granite under heating/cooling cycles and water freeze-thaw condition. Int J Rock Mech Min Sci 45:1164–1175. https://doi.org/10.1016/j.ijrmms.2008.01.002

Tan X, Chen W, Yang J, Cao J (2011) Laboratory investigations on the mechanical properties degradation of granite under freeze-thaw cycles. Cold Reg Sci Technol 68:130–138. https://doi.org/10.1016/j.coldregions.2011.05.007

Wang J, Zhang Q, Song Z, Zhang Y (2019) Creep properties and damage constitutive model of salt rock under uniaxial compression. Int J Damage Mech. https://doi.org/10.1177/1056789519891768

Wang S-R, Chen Y-L, Ni J, Zhang M-D, Zhang H (2019) Influence of freeze-thaw cycles on engineering properties of tonalite: examples from China. Adv Civil Eng. https://doi.org/10.1155/2019/3418134

Xia C, Lv Z, Li Q, Huang J, Bai X (2018) Transversely isotropic frost heave of saturated rock under unidirectional freezing condition and induced frost heaving force in cold region tunnels. Cold Reg Sci Technol 152:48–58. https://doi.org/10.1016/j.coldregions.2018.04.011

Yang X, Jiang A, Li M (2019) Experimental investigation of the time-dependent behavior of quartz sandstone and quartzite under the combined effects of chemical erosion and freeze-thaw cycles. Cold Reg Sci Technol 161:51–62. https://doi.org/10.1016/j.coldregions.2019.03.008

Yavuz H, Altindag R, Sarac S, Ugur I, Sengun N (2006) Estimating the index properties of deteriorated carbonate rocks due to freeze-thaw and thermal shock weathering. Int J Rock Mech Min Sci 43:767–775. https://doi.org/10.1016/j.ijrmms.2005.12.004

Zhang SJ, Lai YM, Zhang XF, Pu YB, Yu WB (2004) Study on the damage propagation of surrounding rock from a cold-region tunnel under freeze-thaw cycle condition. Tunn Undergr Space Technol 19:295–302. https://doi.org/10.1016/j.tust.2003.11.011

Zhang Y, Shao J, Xu W, Jia Y (2016) Time-dependent behavior of cataclastic rocks in a multi-loading triaxial creep test. Rock Mech Rock Eng 49:3793–3803. https://doi.org/10.1007/s00603-016-0948-6